

# Deep Atmospheric Response to the North Pacific Oceanic Subtropical Front in Spring

FUMIAKI KOBASHI

*Faculty of Marine Technology, Tokyo University of Marine Science and Technology, Tokyo, Japan*

SHANG-PING XIE

*International Pacific Research Center, and Department of Meteorology, University of Hawaii at Manoa, Honolulu, Hawaii*

NAOTO IWASAKA

*Faculty of Marine Technology, Tokyo University of Marine Science and Technology, Tokyo, Japan*

TAKASHI T. SAKAMOTO

*Frontier Research Center for Global Change, Japan Agency for Marine-Earth Science and Technology, Kanagawa, Japan*

(Manuscript received 2 November 2007, in final form 12 March 2008)

## ABSTRACT

The North Pacific subtropical front (STF) is a zone of high sea surface temperature (SST) gradients located around 25°N in the western basin and is most pronounced in spring. The STF's atmospheric effects are investigated using satellite observations and an atmospheric reanalysis. During April–May along the STF, surface wind stress curl turns weakly cyclonic in the general background of anticyclonic curls. Atmospheric column-integrated water vapor displays a pronounced meridional maximum along this surface trough, suggesting a deep vertical structure. Cyclonic wind curls occur intermittently at intervals of a few days along the STF in subsynoptic low pressure systems accompanying larger, synoptic highs in the main storm track to the north. In the subsynoptic surface lows, convective rain takes place with deep upward motion moistening the entire troposphere. The lows are enhanced by condensational heating, leading to the formation of weak cyclonic wind curls. The lows display vertical structure characteristic of baroclinic instability, suggesting that they are triggered by the passage of synoptic migratory highs and grow on the baroclinicity anchored by the SST front. The cyclonic wind curls appear to be related to a cloud/rainband associated with the so-called pre-baiu/meiyu front in May.

## 1. Introduction

Surface wind fields over the subtropical North Pacific are characterized by anticyclonic vorticity with the westerlies to the north and the northeast trade winds to the south. The anticyclonic wind stress curls drive the basin-scale subtropical gyre. About 40 years ago, Yoshida and Kidokoro (1967a,b) found a weak local minimum of anticyclonic vorticity in the midst of the subtropical gyre during winter and spring, based on an analysis of seasonal-mean wind stress computed by

Hidaka (1958). They suggested that this trough of anticyclonic wind curl produces an eastward current called the subtropical countercurrent (STCC), which was discovered by Uda and Hasunuma (1969) from direct current meter measurements and geostrophic calculations. Although the wind curl trough is found only during winter and spring in Yoshida and Kidokoro's (1967a,b) analysis, the STCC appears to persist throughout the year (Uda and Hasunuma 1969; White et al. 1978).

Many studies of the formation mechanisms for STCC have followed. Using an ocean general circulation model (GCM), Takeuchi (1984) produced a STCC using wind stress forcing without the wind curl trough, indicating that the wind curl trough of Yoshida and Kidokoro is not essential for the STCC. Recent theo-

---

*Corresponding author address:* Fumiaki Kobashi, Tokyo University of Marine Science and Technology, Faculty of Marine Technology, Etchujima 2-1-6, Koto-ku, Tokyo 135-8533, Japan.  
E-mail: kobashi@kaiyodai.ac.jp

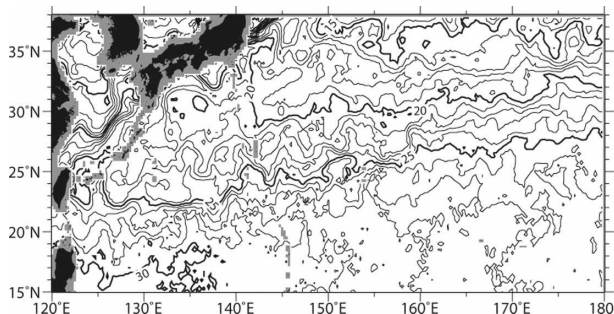


FIG. 1. Weekly mean TMI SST for 30 April–6 May 2000, contoured every 1°C.

retical (Kubokawa 1999) and numerical (Kubokawa and Inui 1999) studies show that the STCC is associated with distinct potential vorticity structures caused by the circulation of mode waters in the ventilated thermocline, a mechanism that has won support from observations (Aoki et al. 2002; Kobashi et al. 2006). This mechanism does not require an anticyclonic curl trough but generates an STCC with smooth wind forcing.

There have been no follow-up studies since Yoshida and Kidokoro (1967a,b) to reexamine the wind curl trough that they reported. It is unclear whether their wind curl trough is a robust feature of the subtropical gyre or an artifact of noisy data of Hidaka (1958). Figure 1 shows a weekly mean map of satellite-derived sea surface temperature (SST), which features a sharp SST front in the STCC region. The SST front extends from the east of Taiwan to the central North Pacific between 20° and 30°N, slightly tilting northward toward the east. The magnitude of the SST gradients is comparable in strength to the Kuroshio Front south of Japan and its extension to the east. This SST front is called the Subtropical Front<sup>1</sup> (STF) (Roden 1975). Recent satellite observations reveal robust air–sea coupling over such sharp SST fronts throughout the World Ocean (Xie 2004). Over the northwest Pacific, SST fronts associated with the Kuroshio and its extension affect the atmosphere and cause significant changes in surface wind (Xie et al. 2002; Nonaka and Xie 2003). These studies suggest a possible atmospheric response to the STF, which may imprint on the surface wind.

The present paper examines surface wind fields over the subtropical northwest Pacific using the Quick Scatterometer (QuikSCAT) vector wind observations that have accumulated since 1999. Our results confirm the wind curl trough of Yoshida and Kidokoro (1967a,b)

<sup>1</sup> This subtropical front is located within the surface mixed layer and is different in nature from the subtropical front associated with the STCC, which is found at the subsurface depth of 100–200 m (Uda and Hasunuma 1969).

and show that the wind curls near the STCC turn cyclonic during spring. We then proceed to study the three-dimensional structure of the atmosphere and processes that lead to the formation of these cyclonic wind curls in the subtropical gyre, using an atmospheric reanalysis product. We show that the atmospheric response to the STF has a deep vertical structure, distinct from that near other SST fronts over the cool ocean, as reviewed in Xie (2004).

The remainder of the paper is organized as follows: The data and processing procedure are described in section 2. Section 3 confirms the existence of the wind curl trough along the STF from satellite observations. Section 4 analyzes the spatiotemporal structure of the surface trough and infers the mechanisms for its development. Section 5 is a summary and discusses possible feedback on the STCC and other implications.

## 2. Data

This study uses surface vector wind velocity measured by the QuikSCAT, SST, columnar water vapor, and precipitation measured by the Tropical Rainfall Measuring Mission (TRMM) Microwave Imager (TMI) from August 1999 to December 2006. Both products are processed by Remote Sensing Systems onto 3-day running mean maps on a 0.25° grid. We compute wind stress based on drag coefficients of Kondo (1975) and calculate the curl by applying a spatial running mean with 1° latitude and 3° longitude to extract the large-scale vorticity structure.

We use the Japanese 25-yr Reanalysis (JRA-25), which is produced jointly by the Japan Meteorological Agency (JMA) and Central Research Institute of Electric Power Industry (CRIEPI). The JRA-25 uses a T106 global spectral forecast model with 40 vertical levels and a three-dimensional variational data assimilation method (Onogi et al. 2007). The JRA-25 covers a main period from 1979 to 2004, but continues to be updated for the subsequent period using the same real-time climatic assimilation system, the JMA Climate Data Assimilation System (JCDAS). This study uses 6-hourly fields of air temperature, specific humidity, and horizontal and vertical velocities available on a 1.25° grid at 12 vertical levels (1000, 925, 850, 700, 600, 500, 400, 300, 250, 200, 150, and 100 hPa). Six-hourly surface variables (wind velocity and stress vectors, air temperature, specific humidity, sea level pressure, and precipitation rate) are available on the T106 Gaussian grid (approximately 1.125° in spacing). We analyze the JRA-25 data for the period of the satellite observations from January 2000 to December 2006.

We use vertical velocity instead of pressure vertical velocity. The vertical velocity  $w$  is derived from the

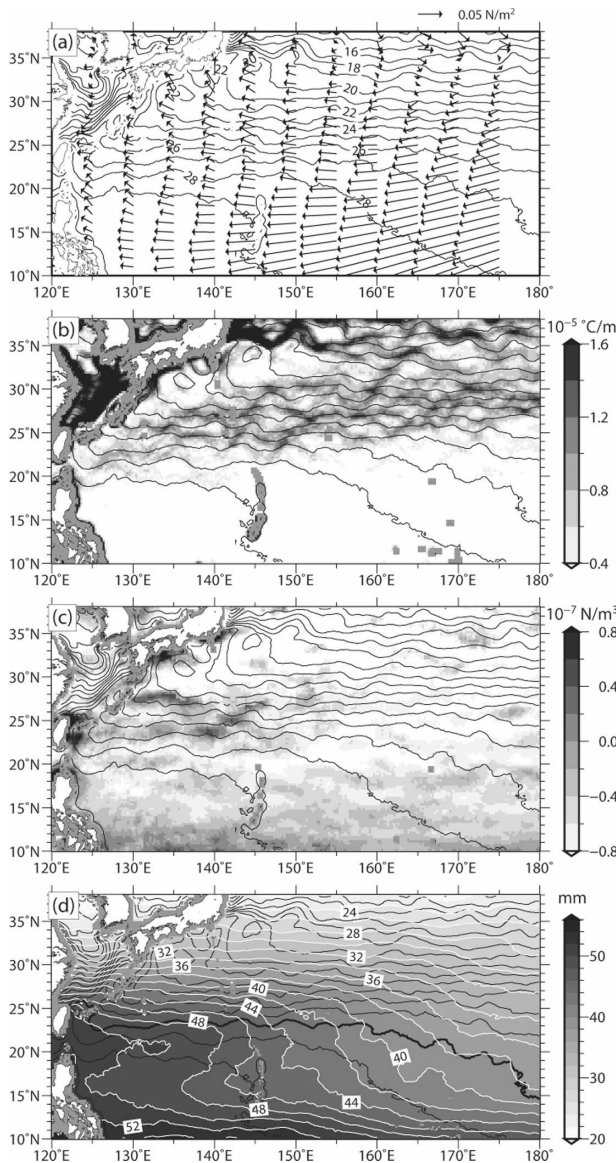


FIG. 2. May climatology from satellite observations for (a) vector wind stress, (b) magnitude of SST gradient, (c) wind stress curl, and (d) columnar water vapor, along with SST in contours. A thick contour in (d) marks the 27°C isotherm.

pressure vertical velocity  $\omega$  by the approximate relationship for synoptic scales under the hydrostatic approximation  $w = -\rho g \omega$ , where  $\rho$  is the air density and  $g$  is the gravity acceleration (Holton 2004).

### 3. Characteristics of cyclonic curls

This section examines the spatial and seasonal variations in QuikSCAT wind stress. Figure 2 shows the May climatology of SST, the magnitude of its gradient, wind stress and its curl, and columnar water vapor, all de-

rived from satellite data. The magnitude of the SST gradient is calculated from the monthly mean SST using  $\sqrt{(\partial \text{SST}/\partial x)^2 + (\partial \text{SST}/\partial y)^2}$ . The STF is clearly identified with a zone of large SST gradients between 20° and 30°N. The wind stress curl is generally anticyclonic (negative) over the subtropical region, but there is a band of local minimum in anticyclonic curl with some narrow cyclonic (positive) curl between 22° and 28°N west of about 155°E. The anticyclonic curl trough is approximately collocated with the STF, associated with a weakening of the easterly trade winds south of the STF around 23°N. The columnar water vapor map features a tongue-like band of high columnar water vapor that extends eastward to 155°E between 18° and 26°N. This high moisture band is located in the area of high SST >27°C and is slightly displaced south of the wind curl trough and the STF.

Figure 3 shows the seasonal variations in the meridional profiles of SST, magnitude of the SST gradient, wind stress and wind stress curl, columnar water vapor, and precipitation obtained from the zonal average between 135° and 145°E. The same figures are also made from the zonal average for every 5° longitude bin between 135° and 155°E, and the results are rather insensitive to the longitude. The STF appears in late fall to the following early summer, anchored between 22° and 28°N presumably by the STCC and the associated subsurface front. The STF seasonal cycle agrees with the results of Roden (1980) based on satellite infrared measurements.

The wind curl trough exhibits a clear seasonality. The subtropical region is occupied by anticyclonic curl throughout the year, except at lower latitudes where cyclonic curls march north from 15°N in July to 22°N in September in association with the development of the northwest Pacific summer monsoon (Ueda and Yasunari 1996). The anticyclonic curl decreases in the STF region from April to May with a pronounced meridional minimum in May. This curl trough is coincident with the seasonal intensification of the SST gradient in the STF from April and May. A careful look indicates that, as the maximum SST gradient migrates northward from 25°N in April to 27°N in May, the center of the wind curl trough also seems to move northward, maintaining its position on the southern flank of the front. These results from satellite observations are confirmed from the JRA-25 data (not shown).

The wind curl trough during April–May is coincident with the abrupt increase in columnar water vapor (Fig. 3c). Although the columnar water vapor shows generally a seasonal evolution similar to that of SST, its abrupt increase from April to May does not seem to follow a similar SST change. This abrupt increase in

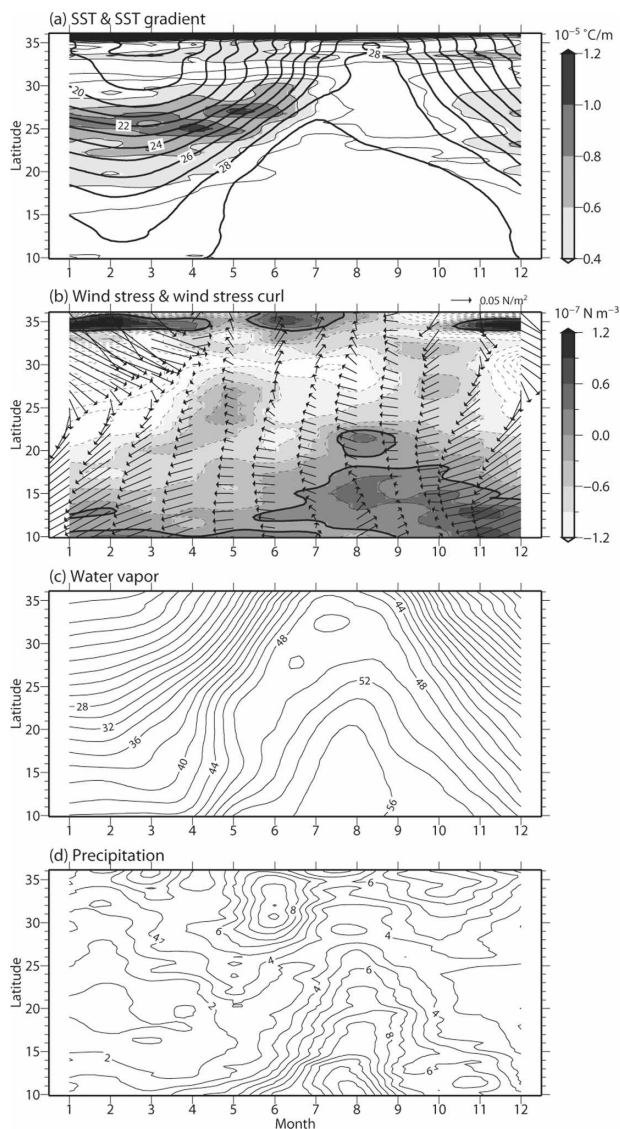


FIG. 3. Satellite-observed seasonal cycle as represented in time-latitude sections of (a) SST (thick contours) and magnitude of the SST gradient (shading), (b) vector wind stress and wind stress curl (zero contours thickened), (c) columnar water vapor (mm), and (d) precipitation ( $\text{mm day}^{-1}$ ), zonally averaged between  $135^{\circ}$  and  $145^{\circ}\text{E}$ .

columnar water vapor is related to the formation of the eastward extending, high moisture tongue in Fig. 2d.

The wind curl trough is also concurrent with a weak but noticeable increase of precipitation over the STF in May (Fig. 3d). The precipitation occurs with some meridional peaks over the STF and is seemingly distinguished from a much stronger rainband lying to the north of  $28^{\circ}\text{N}$ , which is associated with the bai/meiyu front with a maximum peak at June (e.g., Wang and LinHo 2002).

There are other noteworthy features in the subtropi-

cal wind curl. Broad anticyclonic curls weaken in October, and there is a similar but weaker trough centered at  $27^{\circ}\text{N}$ . There are strong cyclonic curls around  $35^{\circ}\text{N}$  almost year-round over the Kuroshio south of Japan, as can be seen from Fig. 2c. Similar cyclonic curls are found in the winter Kuroshio in the East China Sea (Xie et al. 2002) and in the Gulf Stream (Chelton et al. 2004; Xie 2004). This study focuses on the STF region in spring.

We have also investigated wind curl fields using monthly climatology based on long-term ship observations from the International Comprehensive Ocean–Atmosphere Dataset (ICOADS) and found a weak wind curl trough in spring in the STF region. The wind curl trough is also present in a high-resolution coupled GCM jointly developed by the Center for Climate System Research (CCSR) of the University of Tokyo, the National Institute for Environmental Studies (NIES), and the Frontier Research Center for Global Change (FRCGC) of the Japan Agency for Marine–Earth Science and Technology. The atmosphere has T106 spectral resolution with high vertical resolution in the planetary boundary layer, while the ocean has  $0.28^{\circ}$  ( $0.19^{\circ}$ ) horizontal (meridional) resolution (Hasumi and Emori 2004). We use 3-yr output from 71 to 73 model years of a control-run simulation (Sakamoto et al. 2005). Consistent with satellite observations, the model reproduces a narrow band of cyclonic wind curl and a high moisture tongue along the southern flank of the STF (not shown). The wind curl trough also has a clear seasonality—well defined during April–May. The overall agreement between the results from independent observations and the model indicates that the wind curl trough is a robust feature in the STF region.

The present study thus confirms the wind curl trough in the STF region, previously reported by Yoshida and Kidokoro (1967a,b). Here we note several differences from their studies. Whereas Yoshida and Kidokoro (1967a,b) reported the presence of the trough in both winter and spring and extending farther toward the east to  $140^{\circ}\text{W}$ , our trough is present only in spring and is confined to the western part of the subtropical gyre. Probably the differences are attributable to the data used. The Hidaka (1958) wind data that Yoshida and Kidokoro (1967a,b) used are based on sparse ship observations, whereas satellite observations have much superior space–time sampling. In addition, the Hidaka data are gridded seasonally on a  $5^{\circ}$  grid in longitude and latitude, which may be inadequate to resolve the wind curl trough properly in the STF region.

The cyclonic curl in the STF region appears different from the prevailing wind adjustment to SST fronts elsewhere, as reviewed in Xie (2004). A vertical mixing

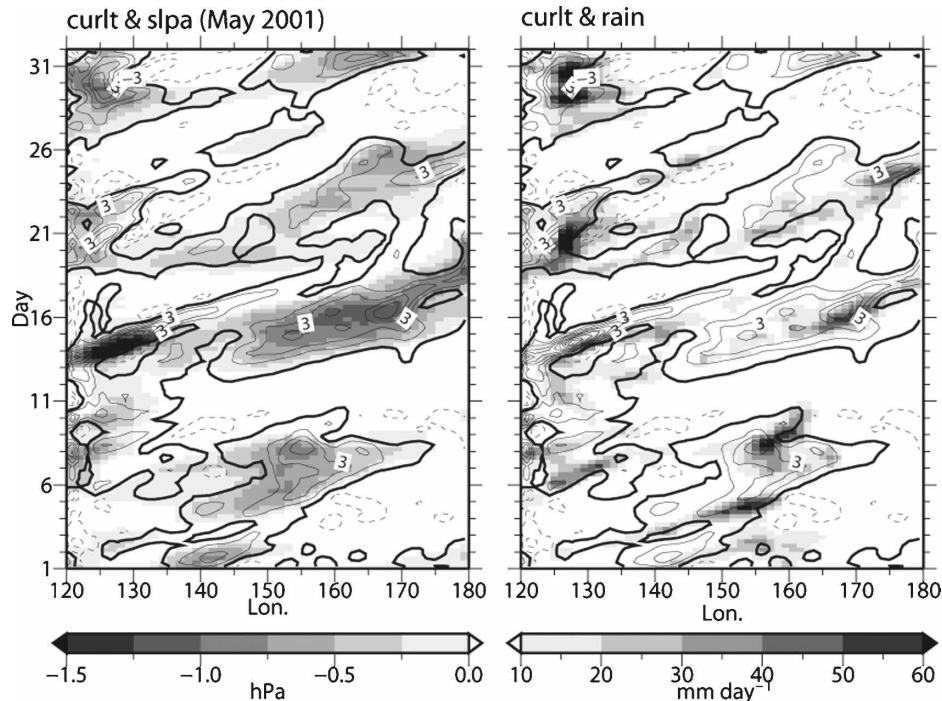


FIG. 4. Time-longitude diagrams of wind stress curl (contours at intervals of  $3 \times 10^{-7} \text{ N m}^{-3}$ ) along with (left) sea level pressure anomaly and (right) rain rates (gray shading). These are obtained from a meridional average of the JRA-25 data between  $23^{\circ}$  and  $27^{\circ}\text{N}$  and then smoothed with a 12-h moving average.

mechanism (Wallace et al. 1989) is considered important in the latter type of atmospheric adjustment, as observed along the Kuroshio (Xie et al. 2002) and Extension (Nonaka and Xie 2003; Tokinaga et al. 2006). In this mechanism, an increase in SST reduces the static stability of the near-surface atmosphere and intensifies the vertical mixing, bringing fast moving air aloft down to the sea surface and accelerating the surface wind. Thus, surface winds blowing parallel to the SST front are accelerated (decelerated) on the warm (cold) sides of the SST front, causing a curl of the surface wind field (Chelton et al. 2001, 2004; O'Neill et al. 2003). Indeed, cyclonic wind curls are generated around  $35^{\circ}\text{N}$  along the Kuroshio south of Japan in the prevailing westerlies (Fig. 3b). Over the STF region, however, the prevailing winds are easterly (Fig. 2a). The wind adjustment by the vertical mixing mechanism would accelerate (decelerate) the easterlies on the southern (northern) flank of the SST front, generating an anticyclonic wind curl, opposite to what is observed. Some other mechanisms are responsible for the cyclonic wind curl along the STF.

#### 4. Structures and mechanisms

This section examines spatiotemporal characteristics of the wind curl trough using JRA-25. Figure 4 shows

time-longitude diagrams in May 2001 of wind stress curl, rain rate, and sea level pressure, meridionally averaged over the trough region between  $23^{\circ}$  and  $27^{\circ}\text{N}$ . For sea level pressure, before calculating the meridional average, we subtract a  $10^{\circ}$  meridional moving average from the original data to remove the large-scale background field. Although only results for 2001 are shown, similar features are seen during other years.

In the STF region, cyclonic wind curls occur intermittently and propagate eastward with a typical period of several days. The cyclonic curl is accompanied by rain and low sea level pressure, suggesting a deep structure in the atmosphere. Indeed, JRA-25 indicates that precipitation in this region is due largely to convective precipitation rather than large-scale condensation. The precipitation over the STF is consistent with the local increase in rain observed by TRMM satellite (Fig. 3d).

##### a. Vertical structure

This subsection investigates the vertical structure of the cyclonic wind curl near the STF using JRA-25. For this, we make two composites based on the May time series of wind curl at  $142.875^{\circ}\text{E}$  (in Fig. 4) for seven years: one by averaging the data when positive curl values exceed one standard deviation and the other by

averaging the data when the curl is negative. The former represents the mean structure for the cyclonic wind curl; the latter the absence of the cyclonic curl. Note that our results are not sensitive to the choice of the reference longitude; the same results are obtained at other nearby longitudes. A close inspection of daily surface weather maps published by the JMA indicates that three events of cyclonic curl are typhoons that formed to the south and moved to the STF region. These typhoons (during 10–13 May 2000, 18–20 May 2002, and 23–25 May 2003) are excluded from the analysis. Out of 868 6-hourly maps, 81 and 493 are included in the strong cyclonic and anticyclonic curl composites, respectively.

Figure 5 shows the composite meridional profiles of SST and surface air temperature (SAT) and the composite latitude–height sections of potential temperature and wind velocity. In both composites, the meridional variations in SAT follow well those in SST (Fig. 5a), and an air temperature front is anchored by the STF between 21° and 29°N within the atmospheric boundary layer below 925 hPa (Figs. 5a,b,d). Thus, the STF maintains surface baroclinicity of the atmosphere. It is noted that the temperature front is also recognized as the front of equivalent potential temperature because of the contrast between warm, wet air to the south and cold, dry air to the north.

Although there is no notable difference in SST (Fig. 5a), the distributions of wind and temperature are quite different between the two composites. When the cyclonic curl is absent at the surface, southerly winds are dominant at the surface in the STF region (Fig. 5b). On the other hand, when the cyclonic curl is present, northerly winds blow from the north over the STF and converge with the southerly winds, leading to a strong upward motion around 24°N (Figs. 5d,e). The upward motion is consistent with the result, from Fig. 4, that the cyclonic curl is associated with low sea level pressure. The SAT decreases (increases) significantly north (south) of the wind convergence as a result of cold (warm) advection in the boundary layer (Fig. 5a).

Figure 6 shows the cyclonic–anticyclonic composite difference. The surface wind convergence near the STF is caused by both the northerly winds and the intensified southerly winds. The upward motion occurs mainly over the southern, warm flank of the STF between 21° and 26°N and reaches the 200-hPa level with a maximum upward velocity of  $2.6 \text{ cm s}^{-1}$  around 300 hPa (Fig. 5e), causing large changes in the circulation of the upper troposphere (Fig. 6a). The upward motion is coincident with a significant increase in moisture, especially in the lower troposphere (Fig. 6b), and a local maximum in convective rain (Fig. 6c). Another remark-

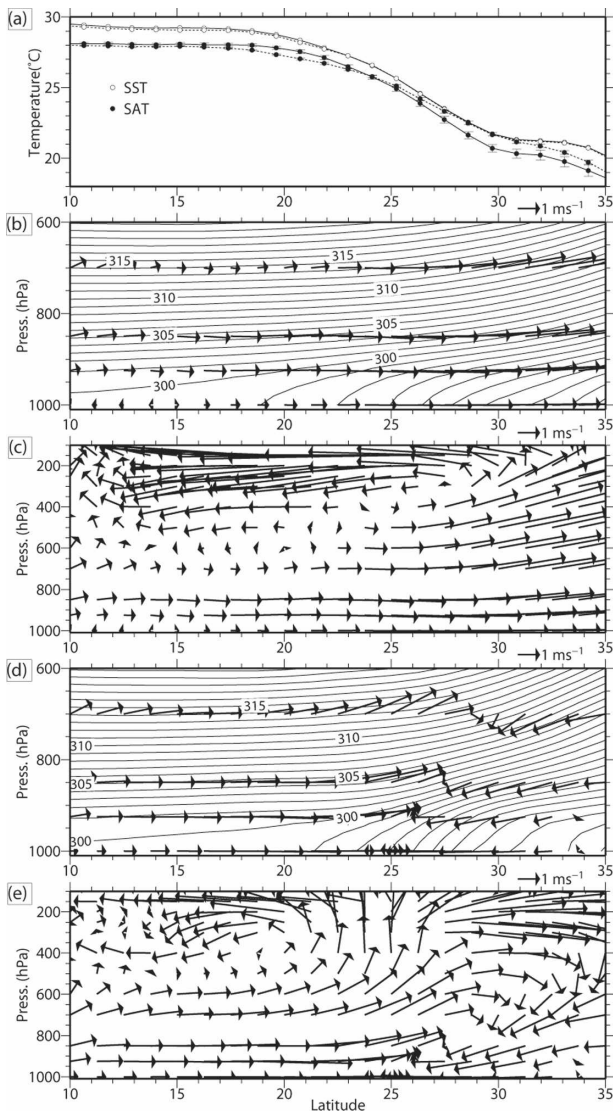


FIG. 5. (a) Meridional profiles at 142.875°E of SST and SAT in the cyclonic (solid lines) and anticyclonic (dashed lines) curl composites, along with 95% confidence intervals for the SAT. Latitude–height sections of meridional and vertical winds (vectors) and potential temperature (K) (contours) for (b), (c) the anticyclonic and (d), (e) the cyclonic curl composite. These are derived from JRA-25. The vertical wind speed is multiplied by 100.

able feature for the cyclonic curl is the presence of a downward motion to the north of 30°N below 200 hPa, accompanied by the decrease in tropospheric moisture and convective rain.

The increase in moisture occurs within the entire air column between 21° and 26°N because of the moisture supply by the upward motion. Specific humidity forms a broad meridional maximum above the atmospheric boundary layer (not shown), consistent with the humid tongue in satellite-observed columnar water vapor (Fig.

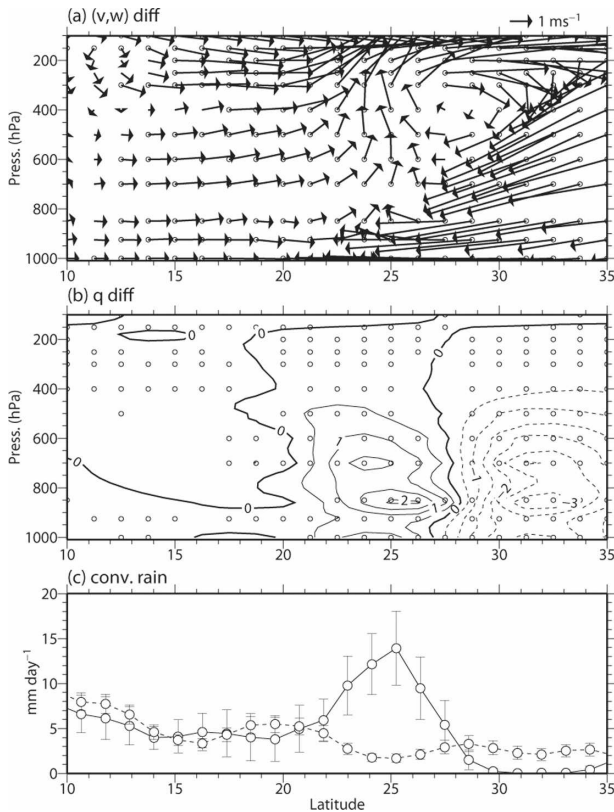


FIG. 6. Cyclonic-anticyclonic curl composite differences of (a) meridional and vertical winds and (b) specific humidity ( $\text{g kg}^{-1}$ ) at  $142.875^\circ\text{E}$ : open circles in (a) and (b) show grid points of significant difference with confidence greater than 95%; the vertical wind speed is multiplied by 100. (c) Meridional profiles of convective rain rate ( $\text{mm day}^{-1}$ ) in the cyclonic (solid line) and the anticyclonic (dashed line) curl composites, along with 95% confidence intervals. These are derived from JRA-25.

2d). The latter lends strong support that the surface cyclonic curls near the STF are associated with deep atmospheric adjustment.

The convective rain indicates latent heating to the atmosphere over the STF. This is confirmed by calculating the apparent heat source  $Q_1$  and the apparent moisture sink  $Q_2$  (e.g., Yanai et al. 1973; Yanai and Tomita 1998), defined as

$$Q_1 = C_p \left( \frac{p}{p_0} \right)^{R/C_p} \left( \frac{\partial \theta}{\partial t} + \mathbf{v} \cdot \nabla \theta + \omega \frac{\partial \theta}{\partial p} \right)$$

and

$$Q_2 = -L \left( \frac{\partial q}{\partial t} + \mathbf{v} \cdot \nabla q + \omega \frac{\partial q}{\partial p} \right).$$

Here  $\theta$  is the potential temperature,  $q$  the mixing ratio of water vapor,  $\mathbf{v}$  the horizontal velocity,  $\omega$  the pressure vertical velocity,  $R$  the gas constant,  $C_p$  the speci-

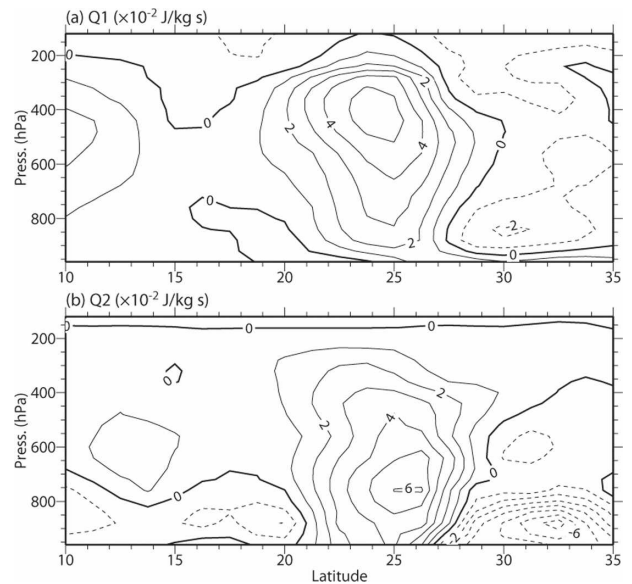


FIG. 7. Latitude-height sections at  $142.875^\circ\text{E}$  of the heat source  $Q_1$  and the moisture sink  $Q_2$  in the cyclonic curl composite, calculated from JRA-25.

fic heat capacity of dry air, and  $L$  the latent heat of condensation. Figure 7 shows the composite latitude-height sections of  $Q_1$  and  $Q_2$  for the cyclonic curl case. The large  $Q_1$  appears over the entire troposphere on the southern flank of the STF, accompanied by  $Q_2$  of similar magnitude, indicating that the heat source mainly comes from the release of latent heat of condensation over the STF. The vertical peak of  $Q_1$  is located above that of  $Q_2$  because of the latent heat transport by strong upward motion there. The convective heating lowers surface pressure and forces deep upward motion. The vertical stretching in the convective region causes cyclonic vorticity in the lower troposphere as observed by QuikSCAT in surface winds.

Figure 8 shows the longitude-height sections of cyclonic-anticyclonic composite differences in geopotential height, vector wind velocity, and potential temperature at  $25^\circ\text{N}$ . The wind stress curl and sea level pressure are also shown in Fig. 8d for the cyclonic curl composite. For sea level pressure, a 15-day moving average is subtracted from the original data to remove the background field.

Because the composites are made with respect to the wind stress curl at  $142.875^\circ\text{E}$ , the surface curl peaks at this reference longitude (Fig. 8d). The axis of the low pressure trough tilts westward with height (Fig. 8a). The upward motion occurs to the east of this trough axis between  $140^\circ$  and  $155^\circ\text{E}$ , where temperature increases except at 600–700 hPa (Fig. 8c). In the downward motion region west of the trough axis, tempera-

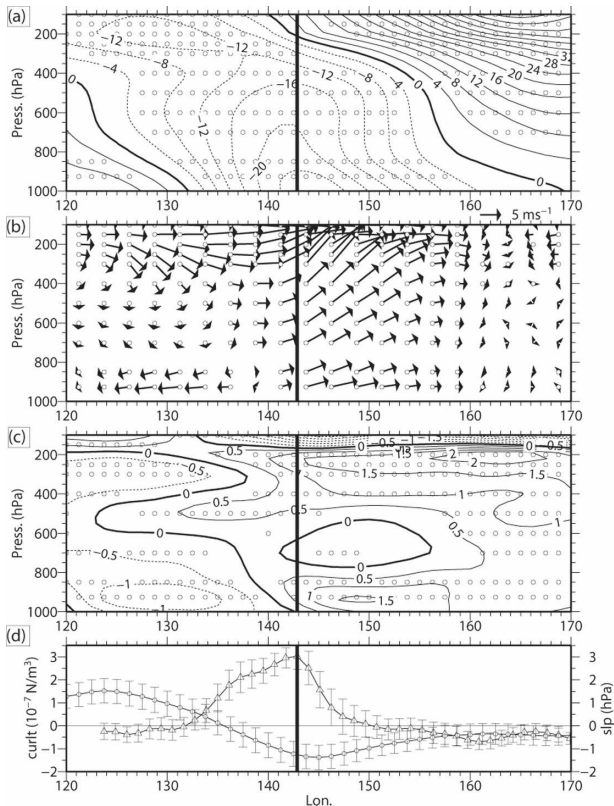


FIG. 8. Cyclonic-anticyclonic curl composite differences of (a) geopotential height (gpm), (b) zonal and vertical winds, and (c) potential temperature (K) at 25°N: open circles in (a)–(c) show grid points of significant difference with confidence greater than 95%; a thick vertical line indicates a reference longitude for the composites; the vertical wind speed is multiplied by 200. (d) Composite profiles of wind stress curl (triangles) and high-pass-filtered sea level pressure (circles) for the cyclonic curl case, along with 95% confidence intervals. These are derived from JRA-25.

ture decreases except at 500 hPa. This pattern of warm air rising and cold air sinking indicates the well-known energy conversion from potential to kinetic energy. Thus, the disturbance with surface cyclonic curl is associated with atmospheric baroclinic instability over the STF. Although the vertical structure somewhat differs from the classical baroclinic instability waves of Eady (1949), the difference may be partly attributable to the latent heating effect in upward motion. In fact, the temperature profile with a cold anomaly at 600–700 hPa in the warm/upwelling sector is similar to the results from Bannon (1986) and Jiang and Gutowski (2000), who investigated baroclinic instability in the presence of condensational heating.

#### b. Cyclonic disturbances over the STF

Not only cyclonic but also anticyclonic disturbances appear along the STF, which are found on both sides of

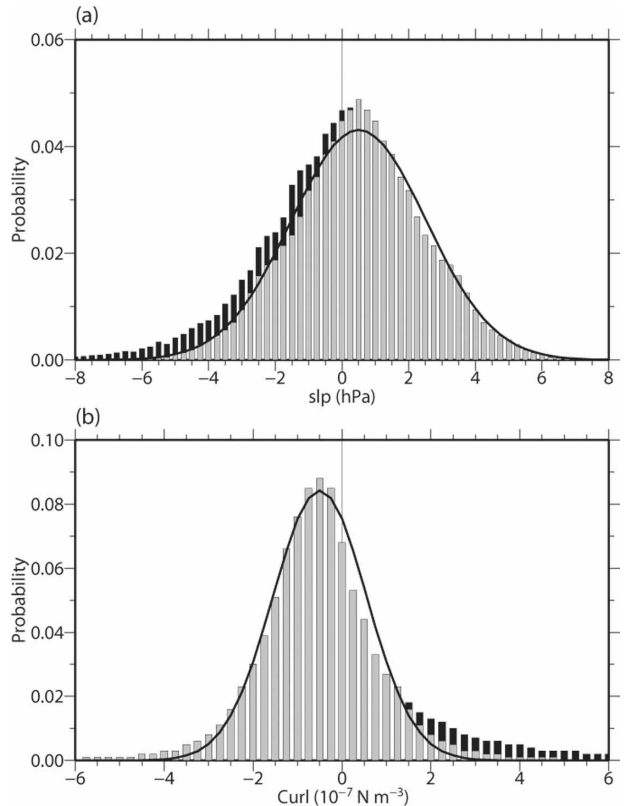


FIG. 9. Probability density function of (a) high-pass-filtered sea level pressure and (b) surface wind stress curl in May in the STF region 23°–27°N, 135°–155°E: dark shading indicates that the probability of low pressures (cyclonic curls) is higher than that of high pressures (anticyclonic curls), and a thick curve denotes a Gaussian fit, assuming a symmetrical distribution of the probability of high pressures (anticyclonic curls) with respect to the center of the probability at 0.5 hPa ( $-0.5 \times 10^{-7} \text{ N m}^{-3}$ ). These are derived from JRA-25.

cyclonic disturbances in Fig. 8. We examine the probability density function of disturbances along the STF using high-pass filtered sea level pressures and surface wind stress curls in May (Fig. 9). The frequency of negative sea level pressure anomalies is generally higher than that of positive ones, with large deviations from the Gaussian distribution for negative anomalies. A similar feature is also seen from the wind stress curls. The frequency of large positive curls ( $>1 \times 10^{-7} \text{ N m}^{-3}$ ) is significantly higher than the Gaussian fit. These probability distribution functions indicate that low pressure systems tend to be well developed and enhanced along the STF.

Figure 10 shows the horizontal distribution of the probability of low pressure disturbances with positive wind curls. The relatively high probability of lows is found in almost the same area as the surface wind curl trough (Fig. 2c), following roughly the large SST gra-

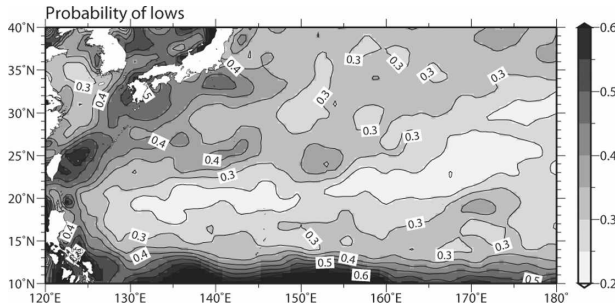


FIG. 10. Distribution of the probability that surface wind stress curls take positive (cyclonic) values in May, calculated from JRA-25.

dient of the STF (Fig. 2b) and hence strong atmospheric baroclinicity. Such high probability is not seen to the north or south away from the STF. Low pressure systems are more intense than the high pressure ones on the STF, and this asymmetry results in the formation of the cyclonic curl band along the STF. Indeed, the mean field computed solely from the days of anticyclonic wind curls does not display a wind curl trough (not shown).

The enhancement of the lows is due to the effect of latent heating. Figure 11 shows the May-mean spatial distribution of the heat source  $\langle Q_1 \rangle$  and moisture sink  $\langle Q_2 \rangle$ , vertically integrated over the lower atmosphere from sea surface to 400 hPa, where the large heat source and moisture sink are observed in the case of cyclonic curls (Fig. 7). The angle brackets denote vertical average:

$$\langle \rangle = \frac{1}{g} \int (\ ) dp.$$

The relatively large  $\langle Q_1 \rangle$  appears along the STF from the northeast of Taiwan to 160°E, with  $\langle Q_2 \rangle$  of similar magnitude, indicating the heat source from the release of latent heat of condensation over the STF. The latent heating enhances atmospheric lows, leading to their frequent occurrence along the STF (Fig. 10).

### c. Horizontal structure

We now turn to the evolution of the disturbance that brings about cyclonic curl on the horizontal plane. Figure 12 shows lagged composite maps of wind stress curl, sea level pressure, and surface wind velocity, with reference to cyclonic wind curl at 142.875°E, 25°N. The temporal high-pass filter is applied to wind velocity and sea level pressure as in Fig. 8d by subtracting a 15-day running mean. A negative (positive) lag denotes a time before (after) the wind curl takes a large cyclonic value at the reference point.

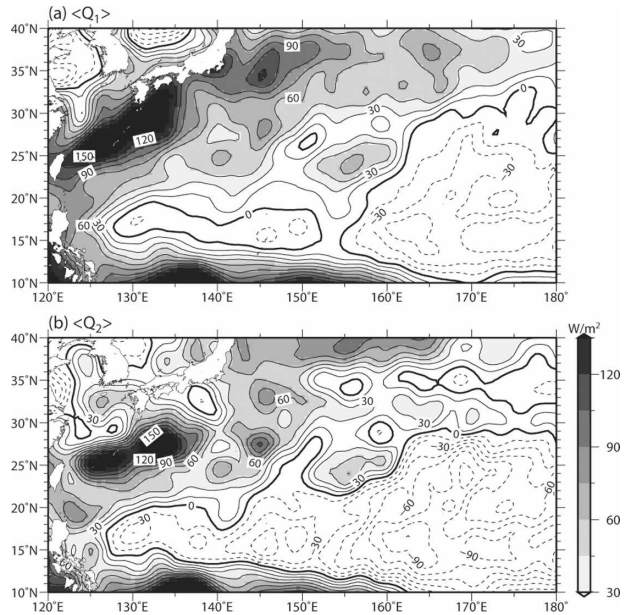


FIG. 11. May climatological mean of (a) the vertically integrated heat source  $\langle Q_1 \rangle$  and (b) the vertically integrated moisture sink  $\langle Q_2 \rangle$ , calculated from JRA-25.

At lag 0, there is a subsynoptic-scale low at the surface in the STF region centered around 27°N, 145°E (Fig. 12c) with anomalous northeasterly (southwesterly) winds to the northwest (southeast). The center of surface cyclonic curl is slightly shifted westward of the low pressure center, as seen from the longitude–height sections in Fig. 8d. The subsynoptic low is located next to a much larger, synoptic-scale high to the northwest centered around 35°N, 135°E. The high pressure is consistent with the downward motion seen there in the composite meridional sections (Fig. 5e). The anomalous northeasterly winds are part of this synoptic high. At the 500-hPa level, the subsynoptic low appears as a pressure trough extending southwestward from a low pressure center east of the surface synoptic high (Fig. 13c).

The subsynoptic low can be traced back to the western edge of the STF around 23°N, 130°E at day  $-2$  as a weak zonal depression in the midst of positive sea level pressure contours (Fig. 12a). (We cannot trace this weak low further back in time.) Weak northerly winds are found on the western flank of the low, apparently as part of the synoptic high centered around 33°N. There is no noticeable upper-level trough above the surface low (Fig. 13a), suggesting that the northerly winds of the synoptic high trigger an initial surface perturbation in the baroclinic zone over the STF.

Consistent with the time–longitude diagrams (Fig. 4), the subsynoptic low propagates eastward. From day  $-2$

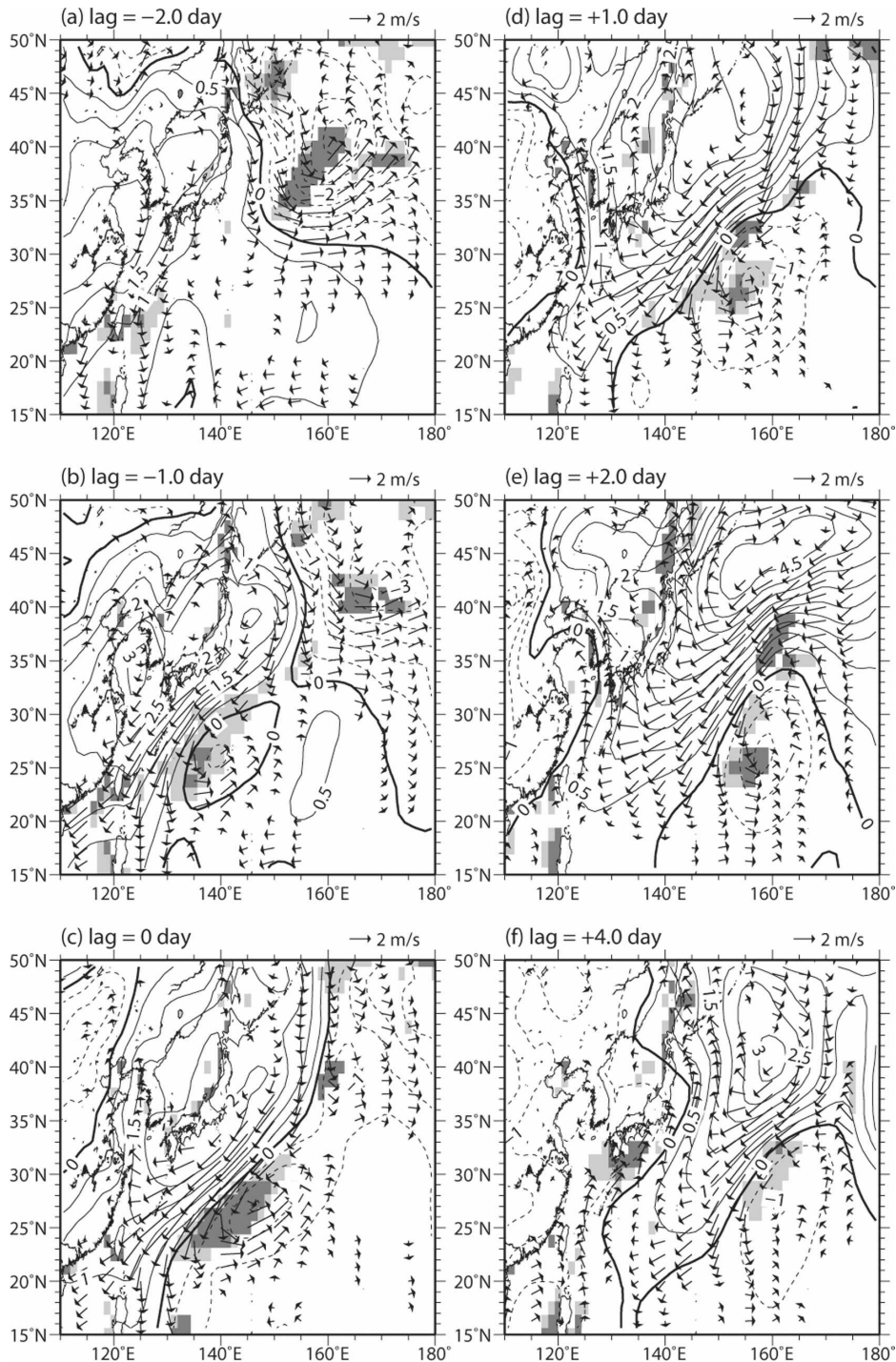


FIG. 12. Time-lagged composite maps of wind stress curl (shading) and temporally high-pass-filtered surface wind and sea level pressure (hPa) (contours) with reference to the cyclonic wind curl at  $142.875^{\circ}\text{E}$  in Fig. 4: wind velocity less than  $0.5 \text{ m s}^{-1}$  is masked out; wind stress curl is shown only for a significantly cyclonic area with 95% confidence, with values greater than  $0.7 \times 10^{-7}$  and  $1.4 \times 10^{-7} \text{ N m}^{-3}$  shaded lightly and darkly over the ocean, respectively. These are derived from JRA-25. See the text for details.

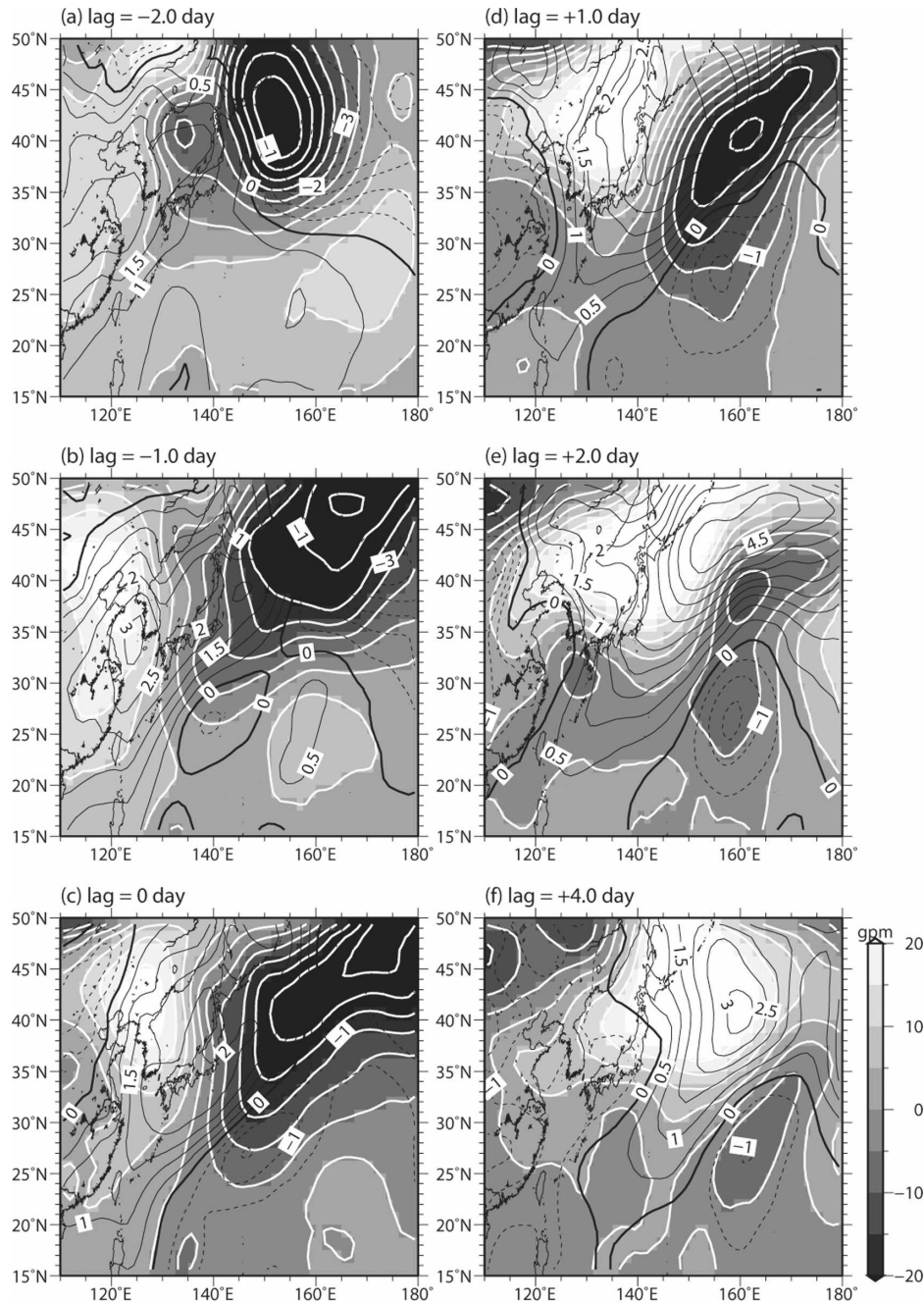


FIG. 13. Time-lagged composite maps of high-pass-filtered geopotential height at 500 hPa (shades) and sea level pressure (hPa) (contours), with reference to the cyclonic wind curl at  $142.875^{\circ}\text{E}$  in Fig. 4. These are derived from JRA-25.

to +2 the low travels along  $26^{\circ}\text{N}$  (the latitude of the STF) and intensifies along with the upper-level trough. During the course, the surface low is attached to the synoptic high to the north, which is a migratory mid-latitude disturbance in the main storm track. The surface low weakens around day +4 and becomes unidentifiable by day +5. East of  $160^{\circ}\text{E}$  the STF still maintains

large SST gradients, but the high moisture tongue disappears with columnar water decreasing rapidly eastward (Fig. 2d). The decay of the surface low and high-moisture tongue is probably due to low SST there (Fig. 2d), which is unfavorable for deep convection. Theoretical studies suggest that latent heating intensifies baroclinic instability (e.g., Bannon 1986).

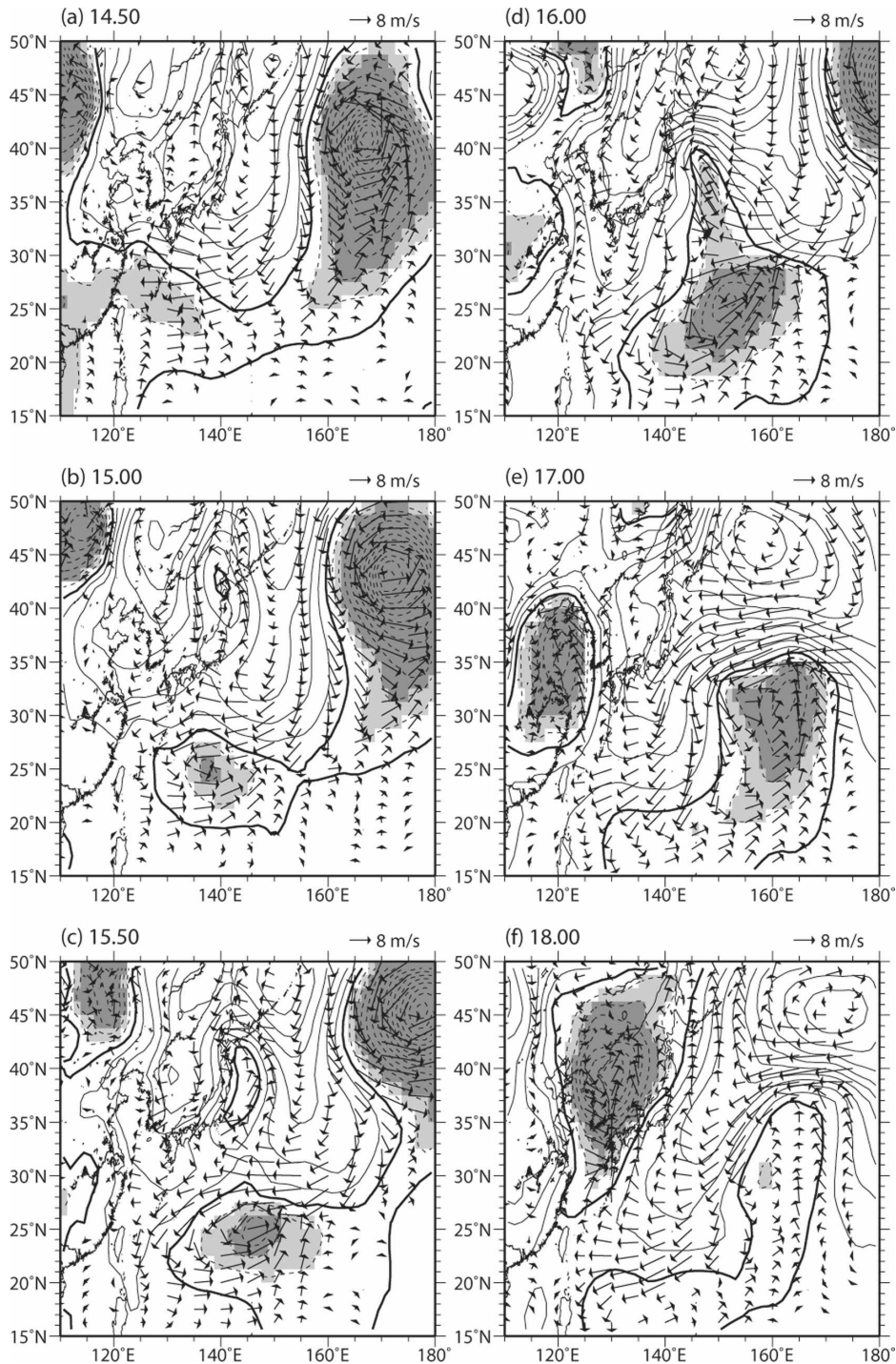


FIG. 14. Instantaneous maps of high-pass-filtered surface wind and sea level pressure (contoured every 2 hPa) during 14–18 May 2005, derived from JRA-25.

The composite evolution of the subsynoptic low is sometimes seen on synoptic weather maps. Figure 14 shows one example during 14–18 May 2005. A weak surface low is first seen at noon on 14 May northeast of Taiwan centered around 26°N, 130°E (Fig. 14a)

with northeasterly (southwesterly) winds to the north (south). The northeasterly winds come from the synoptic high to the north. The surface low then intensifies while propagating eastward along the STF (Figs. 14b,c). After reaching 150°E the low begins moving north on

17 May (Figs. 14d,e), followed by its decay on 18 May (Fig. 14f).

## 5. Summary and discussion

We have used satellite observations and JRA-25 to investigate a trough of anticyclonic wind stress curl over the North Pacific STF first reported by Yoshida and Kidokoro (1967a,b). Our results confirm that there is a meridional minimum in the background of anticyclonic curls between  $22^{\circ}$  and  $28^{\circ}\text{N}$  in the western subtropical gyre. The trough is located on the southern flank of the STF, most pronounced during April–May. Along this curl trough, tropospheric moisture increases, forming a meridional maximum in independent satellite observations. A high-resolution coupled GCM reproduces this surface trough and high moisture tongue along the STF.

Our analysis of JRA-25 reveals that the STF anchors a temperature front and maintains baroclinicity in the atmospheric boundary layer. Cyclonic wind curls in the trough on the STF occur intermittently in low pressure disturbances that propagate eastward with a period of several days and are accompanied with convective rain. The axis of the low pressure trough tilts slightly westward with height, and the upward motion is located to the east. The temperature displays a pattern of warm air rising and cold air sinking, suggestive of baroclinic instability. When the cyclonic curl is present, anomalous northeasterly and southwesterly winds converge onto the STF, forcing upward motion from the surface to 200 hPa. Convective precipitation ensures that the latent heating enhances low pressure disturbance genesis, leading to formation of the cyclonic wind curl along the STF. The vertical transport by the upward motion is responsible for the formation of a high columnar water vapor band observed by satellite.

On the horizontal plane, the low pressure disturbance on the STF is a subsynoptic scale, accompanying a larger, synoptic-scale migratory anticyclone in the storm track to the north. A time-lagged composite analysis shows that the low is first recognized as a smaller-scale low on the western edge of the STF. It is suggested that surface northerly winds of the synoptic high trigger the initial perturbation in the atmospheric baroclinicity zone along the STF. The low intensifies as it travels along the STF, accompanied by a pressure trough in the upper atmosphere. The surface low weakens around  $165^{\circ}\text{E}$  as it moves into cooler waters, which are not conducive to deep convection.

Why does the cyclonic wind curl develop preferentially in April to May? We consider three factors related to the development of the subsynoptic low: storm track activity, atmospheric baroclinicity, and moisture.

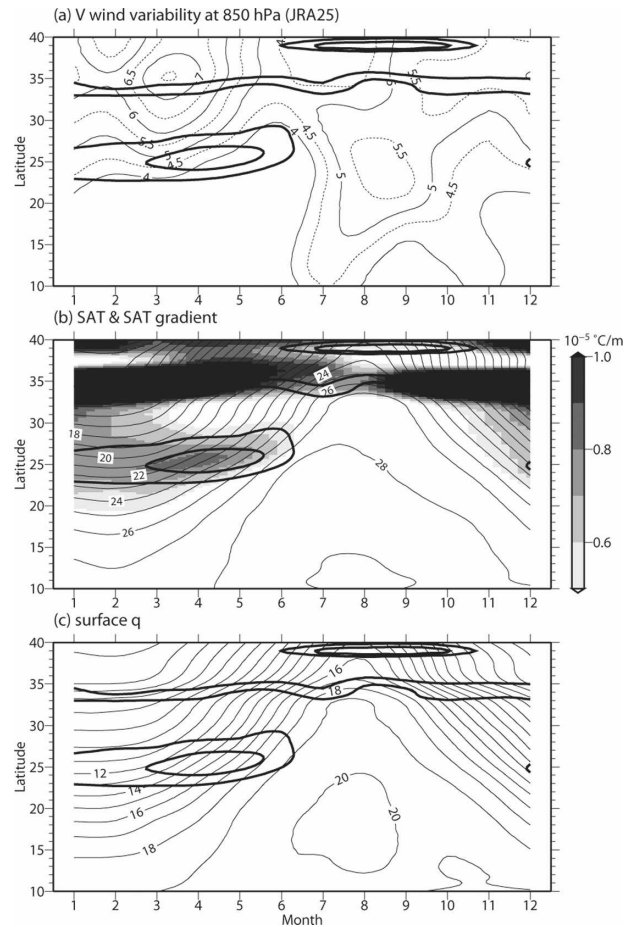


FIG. 15. Seasonal cycle as represented in time–latitude sections from JRA-25: (a) standard deviation of high-pass filtered meridional wind at 850 hPa; (b) SAT (contours) and the magnitude of SAT gradient (shading); and (c) surface specific humidity ( $\text{g kg}^{-1}$ ), zonally averaged between  $135^{\circ}$  and  $145^{\circ}\text{E}$ . Thick contours in (a)–(c) denote SST gradient magnitudes at  $6.0 \times 10^{-6}$  and  $8.0 \times 10^{-6} \text{ }^{\circ}\text{C m}^{-1}$ , marking the STF around  $25^{\circ}\text{N}$ . These are obtained from JRA-25.

Figure 15 shows the standard deviation of high-pass filtered meridional winds at 850 hPa, SAT gradient, and humidity. A major storm track is found around  $35^{\circ}\text{N}$  north of the STF during September to May with two major peaks around January and March, roughly in agreement with the results from previous studies (Nakamura 1992; Nakamura et al. 2004). The atmospheric baroclinicity is large around  $25^{\circ}\text{N}$  from January to June, anchored by the SST front (thick contours in Fig. 15b). The SAT front slightly weakens from April to May despite equally strong SST gradients, possibly a result of baroclinic adjustment. The seasonal evolution of surface moisture roughly follows that of the SAT (SST), with surface humidity increasing rapidly from April to May south of the STF because of the SST

warming. Thus high SST and high humidity conducive to deep convection favor surface trough formation along the STF in April–May. During winter, atmospheric storm activity and baroclinicity are both high but SST is too low, whereas during summer and fall SST is high but the STF is absent. The deep convective nature of atmospheric adjustment to the STF sets it apart from the other type of atmospheric response to SST fronts, ubiquitously observed over a cool ocean, that is characterized by surface wind acceleration (deceleration) on the warmer (colder) flank of a front (Xie 2004).

The northerly winds of synoptic highs advect cold air to the south (Fig. 5a). Such cold air advection sometimes causes significant changes in convective activity in southern warm oceans. This phenomenon has been studied for cold surges off the east coast of China during the winter monsoon (e.g., Lau and Li 1984). Ding and Liu (2001) pointed out that cold air intrusion due to the southward shift of the upper westerly jet induces a rapid amplification of convection in May in the northern South China Sea, triggering the onset of the summer monsoon there. They suggested as a possible mechanism that the enhanced temperature gradient and baroclinicity in the cold surge intensify convection. The convection growing on the increased baroclinicity may resemble the low development on the STF presented in this study, but the enhanced baroclinicity along the STF is due to the SST front rather than cold air advection.

Frequent cyclogenesis occurs northeast of Taiwan (Chen et al. 1991; Adachi and Kimura 2007), to west of the STF. This region of cyclogenesis is identified in Fig. 10 as the frequent appearance of lows. There, the cyclogenesis is due mostly to surface baroclinicity associated with SST gradients across the Kuroshio (Hanson and Long 1985; Xie et al. 2002). Our analysis suggests that these Taiwan cyclones, often accompanying synoptic highs to the north, provide initial perturbations that grow along the STF. Indeed, the time–longitude diagram in Fig. 4 displays some cyclones coming from the Kuroshio region around 123°E.

Our results confirm the existence of an anticyclonic curl trough first suggested by Yoshida and Kidokoro (1967a,b). Whereas Yoshida and Kidokoro explored the possibility that this curl trough drives the STCC, our study focuses on meteorological aspects of the formation of the wind curl trough. In particular, we find enhanced precipitation associated with the wind curl trough (Fig. 3d). This increase in precipitation appears to correspond to the so-called pre-baiu/meiyu front, independently identified from previous meteorological studies. The pre-baiu/meiyu front is manifested as a cloud and rainband and is one of the most remarkable

events in the seasonal march of the East Asia summer monsoon. Using infrared satellite observations and surface weather maps, Kato and Kodama (1992) found a quasi-stationary cloud band in May along 25°N before the onset of the baiu season in Japan, which tends to form south of migratory anticyclones centered and propagating around 30°–40°N. These characteristics are similar to our results. A similar cloud band is also found from Tanaka's (1992) long-term climatology of satellite cloud data. Wang and LinHo (2002) described a similar rainband based on long-term precipitation data. These studies, however, have not investigated the underlying oceanic conditions and the STF in particular. Our results suggest that the STF anchors this pre-baiu/meiyu cloud/rain band, a hypothesis that needs further investigations. While pre-baiu/meiyu subsynoptic lows on the STF display a westward phase tilt with height, some mesoscale lows that develop 1–2 months later on the baiu/meiyu front to the north show an eastward phase tilt (Tagami et al. 2005), possibly indicative of a stronger condensational heating effect.

The JRA-25 captures the trough of anticyclonic wind curls observed by satellite. The horizontal grid spacing of the JRA-25 is approximately 1.125°, barely sufficient to resolve the trough whose meridional scale about 5° (Fig. 2c). It should be noticed, however, that the actual resolution of a numerical model in the sense of ability to represent a given feature is known to be generally 4 to 10 times larger than the grid spacing (Pielke 1991; Grasso 2000; Walters 2000; Durran 2000). Thus, the wind curl trough from the JRA-25 is somewhat smoothed. Indeed, compared to satellite observations (Fig. 2c), the May climatology of surface wind stress curl calculated from the JRA-25 displays a weak and meridionally smoothed wind curl trough. The subsynoptic lows that develop along the STF and are responsible for the curl trough may be more intense in magnitude and smaller in spatial scale in the real world than in the JRA-25.

Although not essential to the formation of STCC (Takeuchi 1984; Kubokawa 1999), the cyclonic wind curl may still influence and feed back onto the STCC. The Hawaiian Lee Countercurrent (HLCC) serves as an example. Although to first order the HLCC is orographically generated by the tall Hawaiian Islands (Xie et al. 2001; Sakamoto et al. 2004), Sasaki and Nonaka (2006) showed from a high-resolution ocean simulation that HLCC-induced SST changes alter wind curl (Hafner and Xie 2003), extending the HLCC far to the west. Similar feedback may be possible in the STCC region, with the STF-induced cyclonic wind curl modifying the STCC through Sverdrup dynamics. For example, the STCC varies on seasonal and interannual

time scales (White et al. 1978; Kobashi and Kawamura 2002), but the mechanism has not been clarified. We need to evaluate the influence of the cyclonic wind curl as well as the potential vorticity dynamics of Kubokawa (1999) and Kobashi et al. (2006) for a fuller understanding of STCC variations.

A similar local minimum of wind curl has also been reported in the subtropical gyre of the North Atlantic (Yoshida and Kidokoro 1967b; Schmitz et al. 1992). Schmitz et al. noticed from wind stress maps that Sverdrup transport streamlines are commonly distorted eastward near 30°N in the western subtropical gyre. The distortion is probably attributable to the existence of a wind curl trough. They further noted that the regional pattern of Sverdrup transport seems to be in agreement with the observed geostrophic flow. The STF exists with large horizontal SST gradients in the North Atlantic (e.g., Voorhis and Hersey 1964; Ullman et al. 2007). The distortion of Sverdrup transport appears to occur roughly along the STF. It would be interesting to explore whether the North Atlantic wind curl trough is formed in the same way as in the North Pacific.

*Acknowledgments.* We thank H. Nakamura for comments and helpful discussion. Careful comments from the anonymous reviewers helped improve an early version of the manuscript. This work is partially supported by the Ministry of Education, Culture, Sports, Science and Technology, Japan [Grant-in-Aid for Young Scientists (B), Nos. 17740305 and 20740267] and by the Japan Society for the Promotion of Science [Grant-in-Aid for Scientific Research (B), No. 17340137], the Japan Agency for Marine–Earth Science and Technology, and the U.S. National Aeronautic and Space Administration and National Science Foundation. The satellite data were obtained from the Remote Sensing Systems website, and the Japanese 25-year Reanalysis (JRA-25) from the website of the Japan Meteorological Agency Global Environment and Marine Department. IPRC publication 524 and SOEST publication 7461.

#### REFERENCES

- Adachi, S., and F. Kimura, 2007: A 36-year climatology of surface cyclogenesis in East Asia using high-resolution reanalysis data. *SOLA*, **3**, 113–116.
- Aoki, Y., T. Suga, and K. Hanawa, 2002: Subsurface subtropical fronts of the North Pacific as inherent boundaries in the ventilated thermocline. *J. Phys. Oceanogr.*, **32**, 2299–2311.
- Bannon, P. R., 1986: Linear development of quasi-geostrophic baroclinic disturbances with condensational heating. *J. Atmos. Sci.*, **43**, 2261–2274.
- Chelton, D. B., and Coauthors, 2001: Observation of coupling between surface wind stress and sea surface temperature in the eastern tropical Pacific. *J. Climate*, **14**, 1479–1498.
- , M. G. Schlax, M. H. Freilich, and R. F. Milliff, 2004: Satellite measurements reveal persistent small-scale features in ocean winds. *Science*, **303**, 978–983, doi:10.1126/science.1091901.
- Chen, S.-J., Y.-H. Kuo, P.-Z. Zhang, and Q.-F. Bai, 1991: Synoptic climatology of cyclogenesis over East Asia, 1958–1987. *Mon. Wea. Rev.*, **119**, 1407–1418.
- Ding, Y., and Y. Liu, 2001: Onset and the evolution of the summer monsoon over the South China Sea during SCSMEX field experiment in 1998. *J. Meteor. Soc. Japan*, **79**, 255–276.
- Durran, D. R., 2000: Comments on “The differentiation between grid spacing and resolution and their application to numerical modeling.” *Bull. Amer. Meteor. Soc.*, **81**, 2478.
- Eady, E. T., 1949: Long waves and cyclone waves. *Tellus*, **1**, 33–52.
- Grasso, L. D., 2000: The differentiation between grid spacing and resolution and their application to numerical modeling. *Bull. Amer. Meteor. Soc.*, **81**, 579–580.
- Hafner, J., and S.-P. Xie, 2003: Far-field simulation of the Hawaiian wake: Sea surface temperature and orographic effects. *J. Atmos. Sci.*, **60**, 3021–3032.
- Hanson, H. P., and B. Long, 1985: Climatology of cyclogenesis over the East China Sea. *Mon. Wea. Rev.*, **113**, 697–707.
- Hasumi, H. and S. Emori, Eds., 2004: Coupled GCM (MIROC) description. K-1 Tech. Rep. 1, Center for Climate System Research, University of Tokyo, 34 pp. [Available online at <http://www.ccsr.u-tokyo.ac.jp/kyosei/hasumi/MIROC/tech-repo.pdf>.]
- Hidaka, K., 1958: Computation of the wind stresses over the oceans. *Rec. Oceanogr. Works Japan*, **4**, 77–123.
- Holton, J. R., 2004: *An Introduction to Dynamical Meteorology*. 4th ed. Academic Press, 535 pp.
- Jiang, W., and W. J. Gutowski, 2000: Moist baroclinic instability in the presence of surface–atmosphere coupling. *J. Atmos. Sci.*, **57**, 2923–2935.
- Kato, K., and Y. Kodama, 1992: Formation of the quasi-stationary Baiu front to the south of the Japan Islands in early May of 1979. *J. Meteor. Soc. Japan*, **70**, 631–647.
- Kobashi, F., and H. Kawamura, 2002: Seasonal variation and instability nature of the North Pacific Subtropical Countercurrent and the Hawaiian Lee Countercurrent. *J. Geophys. Res.*, **107**, 3185, doi:10.1029/2001JC001225.
- , H. Mitsudera, and S.-P. Xie, 2006: Three subtropical fronts in the North Pacific: Observational evidence for mode water-induced subsurface frontogenesis. *J. Geophys. Res.*, **111**, C09033, doi:10.1029/2006JC003479.
- Kondo, J., 1975: Air–sea bulk transfer coefficients in diabatic conditions. *Bound.-Layer Meteor.*, **9**, 91–112.
- Kubokawa, A., 1999: Ventilated thermocline strongly affected by a deep mixed layer: A theory for subtropical countercurrent. *J. Phys. Oceanogr.*, **29**, 1314–1333.
- , and T. Inui, 1999: Subtropical countercurrent in an idealized ocean GCM. *J. Phys. Oceanogr.*, **29**, 1303–1313.
- Lau, K. M., and M. T. Li, 1984: The monsoon of East Asia and its global associations—A survey. *Bull. Amer. Meteor. Soc.*, **65**, 114–125.
- Nakamura, H., 1992: Midwinter suppression of baroclinic wave activity in the Pacific. *J. Atmos. Sci.*, **49**, 1629–1642.
- , T. Sampe, Y. Tanimoto, and A. Shimpo, 2004: Observed associations among storm tracks, jet streams and midlatitude oceanic fronts. *Earth’s Climate: The Ocean–Atmosphere Interaction*, *Geophys. Monogr.*, Vol. 147, Amer. Geophys. Union, 329–346.

- Nonaka, M., and S.-P. Xie, 2003: Co-variations of sea surface temperature and wind over the Kuroshio and its extension: Evidence for ocean-to-atmosphere feedback. *J. Climate*, **16**, 1404–1413.
- O'Neill, L. W., D. B. Chelton, and S. K. Esbensen, 2003: Observations of SST-induced perturbations of the wind stress field over the Southern Ocean on seasonal time scales. *J. Climate*, **16**, 2340–2354.
- Onogi, K., and Coauthors, 2007: The JRA-25 Reanalysis. *J. Meteor. Soc. Japan*, **85**, 369–432.
- Pielke, R. A., 1991: A recommended specific definition of “resolution.” *Bull. Amer. Meteor. Soc.*, **72**, 1914.
- Roden, G. I., 1975: On the North Pacific temperature, salinity, sound velocity, and density fronts and their relation to the wind and energy flux fields. *J. Phys. Oceanogr.*, **5**, 557–571.
- , 1980: On the variability of surface temperature fronts in the western Pacific, as detected by satellite. *J. Geophys. Res.*, **85**, 2704–2710.
- Sakamoto, T. T., A. Sumi, S. Emori, T. Nishimura, H. Hasumi, T. Suzuki, and M. Kimoto, 2004: Far-reaching effects of the Hawaiian Islands in the CCSR/NIES/FRCGC high-resolution climate model. *Geophys. Res. Lett.*, **31**, L17212, doi:10.1029/2004GL020907.
- , H. Hasumi, M. Ishii, S. Emori, T. Suzuki, T. Nishimura, and A. Sumi, 2005: Responses of the Kuroshio and the Kuroshio Extension to global warming in a high-resolution climate model. *Geophys. Res. Lett.*, **32**, L14617, doi:10.1029/2005GL023384.
- Sasaki, H., and M. Nonaka, 2006: Far-reaching Hawaiian Lee Countercurrent driven by wind-stress curl induced by warm SST band along the current. *Geophys. Res. Lett.*, **33**, L13602, doi:10.1029/2006GL026540.
- Schmitz, W. J., Jr., J. D. Thompson, and J. R. Luyten, 1992: The Sverdrup circulation for the Atlantic along 24°N. *J. Geophys. Res.*, **97**, 7251–7256.
- Tagami, H., H. Niino, W. Yanase, and T. Kato, 2005: Characteristics of the Meso- $\alpha$ -scale low on the Baiu front (in Japanese). *Tenki*, **52**, 767–770.
- Takeuchi, K., 1984: Numerical study of the Subtropical Front and the Subtropical Countercurrent. *J. Oceanogr.*, **40**, 371–381.
- Tanaka, M., 1992: Intraseasonal oscillation and the onset and retreat dates of the summer monsoon over East, Southeast Asia and the western Pacific region using GMS high cloud amount data. *J. Meteor. Soc. Japan*, **70**, 613–629.
- Tokinaga, H., and Coauthors, 2006: Atmospheric sounding over the winter Kuroshio Extension: Effect of surface stability on atmospheric boundary layer structure. *Geophys. Res. Lett.*, **33**, L04703, doi:10.1029/2005GL025102.
- Uda, M., and K. Hasunuma, 1969: The eastward subtropical countercurrent in the western North Pacific Ocean. *J. Oceanogr. Soc. Japan*, **25**, 201–210.
- Ueda, H., and T. Yasunari, 1996: Maturing process of the summer monsoon over the western North Pacific: A coupled ocean/atmosphere system. *J. Meteor. Soc. Japan*, **74**, 493–508.
- Ullman, D. S., P. C. Cornillon, and Z. Shan, 2007: On the characteristics of subtropical fronts in the North Atlantic. *J. Geophys. Res.*, **112**, C01010, doi:10.1029/2006JC003601.
- Voorhis, A. D., and J. B. Hersey, 1964: Oceanic thermal fronts in the Sargasso Sea. *J. Geophys. Res.*, **69**, 3809–3814.
- Wallace, J. M., T. P. Mitchell, and C. Deser, 1989: The influence of sea surface temperature on surface wind in the eastern equatorial Pacific: Seasonal and interannual variability. *J. Climate*, **2**, 1492–1499.
- Walters, M. K., 2000: Comments on “The differentiation between grid spacing and resolution and their application to numerical modeling.” *Bull. Amer. Meteor. Soc.*, **81**, 2475–2477.
- Wang, B., and LinHo, 2002: Rainy season of the Asian–Pacific summer monsoon. *J. Climate*, **15**, 386–398.
- White, W. B., K. Hasunuma, and H. Solomon, 1978: Large-scale seasonal and secular variability of the subtropical front in the western North Pacific from 1954 to 1974. *J. Geophys. Res.*, **83**, 4531–4544.
- Xie, S.-P., 2004: Satellite observations of cool ocean–atmosphere interaction. *Bull. Amer. Meteor. Soc.*, **85**, 195–208.
- , W. T. Liu, Q. Liu, and M. Nonaka, 2001: Far-reaching effects of the Hawaiian Islands on the Pacific Ocean–atmosphere system. *Science*, **292**, 2057–2060.
- , J. Hafner, Y. Tanimoto, W. T. Liu, H. Tokinaga, and H. Xu, 2002: Bathymetric effect on the winter sea surface temperature and climate of the Yellow and East China Seas. *Geophys. Res. Lett.*, **29**, 2228, doi:10.1029/2002GL015884.
- Yanai, M., and T. Tomita, 1998: Seasonal and interannual variability of atmospheric heat sources and moisture sinks as determined from NCEP–NCAR Reanalysis. *J. Climate*, **11**, 463–482.
- , S. Esbensen, and J. H. Chu, 1973: Determination of bulk properties of tropical cloud clusters from large-scale heat and moisture budgets. *J. Atmos. Sci.*, **30**, 611–627.
- Yoshida, K., and T. Kidokoro, 1967a: A subtropical countercurrent in the North Pacific—An eastward flow near the subtropical convergence. *J. Oceanogr. Soc. Japan*, **23**, 88–91.
- , and —, 1967b: A subtropical countercurrent (II)—A prediction of eastward flows at lower subtropical latitudes. *J. Oceanogr. Soc. Japan*, **23**, 231–236.